J Fluoresc (2009) 19:211–219
DOI 10.1007/s10895-008-0404-4

ORIGINAL PAPER

Photoluminescence and Photoacoustic Spectroscopies of Fe^{3+} in the $LiGa_5O_8$–$LiGaSiO_4$–$Li_5GaSi_2O_8$ System

Sandra S. Pedro · Ossamu Nakamura · Ricardo B. Barthem · Lilian P. Sosman

Received: 13 June 2008 / Accepted: 28 July 2008 / Published online: 6 August 2008

Abstract This report is devoted to the study of the low and room temperature photoluminescence and photoacoustic spectroscopy of the Fe^{3+} impurity ion in the $LiGa_5O_8$–$LiGaSiO_4$–$Li_5GaSi_2O_8$ system. The sample was obtained by solid-state reaction between β-Ga_2O_3, Li_2CO_3, SiO_2 and appropriated quantities of Fe_2O_3. It was investigated by X-ray diffraction to determine the formed phases and through photoluminescence, excitation and photoacoustic spectroscopy measurements. The broad absorption and emission bands in the visible and near-infrared spectral regions presented by that system constitute the motivation for this study. More specifically, the luminescence occurs over a large interval of wavelengths, between 400 nm and 800 nm.

Keywords Photoluminescence · Excitation · Photoacoustic absorption · Fe^{3+}

S. S. Pedro · L. P. Sosman (✉)
Instituto de Física, Universidade do Estado do Rio de Janeiro,
Rua São Francisco Xavier 524,
Rio de Janeiro, RJ, Brazil
e-mail: sosman@uerj.br

O. Nakamura
Instituto de Física, Universidade Federal da Bahia,
Campus Universitário de Ondina,
Salvador, BA 40210-340, Brazil

R. B. Barthem
Instituto de Física, Universidade Federal do Rio de Janeiro,
Cidade Universitária, Ilha do Fundão,
Rio de Janeiro, RJ 21941-972, Brazil

Introduction

Recent research advances on luminescent materials point to their utility in a wide range of fields that include, among many others, medicine, metrology, short pulse generation, optical communication, sources for non-linear optics, information storage, electronic devices, white emission sources, light emitting diodes and thermoluminescent devices [1–11]. Several inorganic materials doped with transition ions present broad emission and absorption bands in the visible and infrared spectral regions [12, 13]. The optical spectra are generated by couplings between electronic transitions and vibrational modes of hosts. The broad emission bands can be tunable, making these materials very attractive by the emission wavelength choice possibility. The doping of inorganic materials with Fe^{3+} tetrahedrally or octrahedrally coordinated is also attractive [14–23] because allows observable energy transitions in higher and lower energy regions in addition to the broad bands generated in absorption and emission processes.

The Fe^{3+} ion has a d^5 electronic configuration. When the Fe^{3+} ion is surrounded by ligand anions (crystalline field), its energy levels are splitted and the new configuration is described by Tanabe–Sugano diagrams [24, 25]. The d^5 free ion ground energy term, ^6S, is transformed, for low crystal field parameter Dq, in a lower $^6A_1\left(t_2^3e^2\right)$ energy level. The excited energy states are, in increasing order, ^4G and ^4D levels. The ^4G energy term is splitted in $^4T_1\left(t_2^4e\right)$, $^4T_2\left(t_2^4e\right)$ and $^4A_1 + {}^4E\left(t_2^4e\right)$ states. The ^4D term is transformed into the $^4E\left(t_2^4e\right)$ energy level. The optical transitions in Fe^{3+}occur between energy levels with different spin multiplicities, therefore are forbidden and are always associated with weak bands in spectra. Moreover, transitions between energy levels with different electronic configurations originate broad bands. In this work we study the Fe^{3+} impurity ion in the

$LiGa_5O_8$–$LiGaSiO_4$–$Li_5GaSi_2O_8$ system. The ionic radii of Fe^{3+} and Ga^{3+} are both 0.64 Å, while for Li^+ and Si^{4+} are 0.68 Å and 0.42 Å, respectively. The radii values and the similar valence indicate that substitution of Ga^{3+} ions is more likely to be by Fe^{3+} ions. In spite of the proximity of ionic radii values, the probability of introduction of Fe^{3+} in Li^+ sites is low, due to the great difference of charge and electronic configuration between the two cations. On the other hand, lithium valence would cause a large change in atomic positions to compensate charges, and we believe that in our sample (see below) Fe^{3+} ions enter uniquely in Ga^{3+} sites. However, the entrance of Fe^{3+} ion in Li^+ sites has been observed in $LiNbO_3$ [26] and in $LiAlO_2$ [21]. We have observed broad absorption and emission bands in the visible and near-infrared spectral regions at room and low temperatures. The photoacoustic spectra in the visible region are similar to photoluminescence excitation spectra, showing that all visible wavelengths can be used for luminescence excitation in spite of the intensity lost in non-radiative processes. The luminescence spectra show broad bands between 400 nm and 800 nm, which suggests that this system could be used as wide light tunable source, depending on the excitation wavelength. The crystal field and interelectronic parameters values obtained from experimental data and Tanabe–Sugano matrices [24, 25] show that the impurity is in tetrahedral sites and that the interaction between the impurity and its neighborhood is strongly covalent.

Experimental section

Powder samples were produced by solid state reaction from Li_2CO_3, β-Ga_2O_3, SiO_2 and Fe_2O_3 reactants oxides. The reaction can be represented by the following equilibrium equation:

$$0.652\ Li_2CO_3 + \beta{-}Ga_2O_3 + 0.435\ SiO_2 \rightarrow 0.347\ LiGa_5O_8 + 0.173\ Li_5GaSi_2O_8 + 0.086\ LiGaSiO_4 + 0.652\ CO_2$$

The reactants quantities calculated for 2 g of products were 0.3682 g of Li_2CO_3, 1.4322 g of β-Ga_2O_3 and 0.1996 g of SiO_2. In order to doping, 5% of the Ga_2O_3 mass was substituted by 0.0716 g of Fe_2O_3. Raw oxides were mixed during 7 h in an agate mortar and pressed into discs of 0.25 g with diameter of 10 mm and 2 mm thick, under a 2 t charge. Samples were fired in air for 24 h at 800 °C, under atmospheric pressure. The furnace was turn off and the samples were cooled to room temperature inside the furnace by thermal inertia. After this, the samples were pulverized and pressed into discs with 2 t charge again and 72 h firing at 1,000 °C. Then the furnace was turned off and the samples cooled by furnace inertia to room temperature once more. Finally, the samples were inspected in relation to their homogeneity and color. They presented a good homogeneity and the slightly yellow color characteristic of trivalent iron. After the thermal treatment one disc was pulverized and investigated by powder X rays diffraction. The compound formation was investigated with an X Pert Pro PANalytical diffractometer operating at 40 kV and 40 mA, equipped with a cobalt tube monochromator for CuKα radiation (λ= 1.54056 Å). An angular step size of 0.05° was used with a scanning speed of 3°/min, between $10° \leq 2\theta \leq 100°$.

Photoluminescence and excitation spectra were obtained using a 2061 McPherson spectrometer and a RCA 31034 photomultiplier in order to scan the emission, together with an AM505F ARC spectrometer used to select the excitation wavelength. The exciting sources were a 250 W tungsten lamp and a cw 488 nm line from a Laser Ion Technology Ar-ion laser model 5400-220-00. The excitation intensity was modulated at a reference frequency using a PAR 191 variable speed chopper. An EG&G PAR Instrumentation model 5209 lock-in and a Tektronix Model TDS 350 digital oscilloscope were used to acquire and process the primary signal. Low-temperature experiments were performed using a Janis ST-100 gas flow cryostat. The set-up for photoacoustic measurements was composed by a 1 kW xenon lamp (Osram) chopped at 20 Hz (SR 540 variable speed chopper) and an air filled photoacoustic cell supplied with a commercial electret microphone and a quartz window. A Sciencetch 9010 spectrometer was used to select an excitation wavelength between 350 nm and 700 nm. The obtained photoacoustic signal was analyzed with a SR 530 lock-in. Finally, for signal-frequency dependence measurements we have employed the same apparatus but using frequency intervals from 10 to 90 Hz in steps of 2 Hz. All the optical spectra were corrected by the response of the detection system.

The optical transitions observed through photoluminescence and photoacoustic techniques were analyzed using Tanabe–Sugano (TS) energy diagrams [24, 25] and TS matrices, which solutions are listed in Eqs. (1) to (5). They were used to calculate the crystal field Dq and B and C Racah parameters.

$$^6A_1(S) \rightarrow {}^4T_2\left({}^4D\right) = 13B + 5C \tag{1}$$

$$^6A_1\left({}^6S\right) \rightarrow {}^4E\left({}^4D\right) = 17B + 5C \tag{2}$$

$$^6A_1\left({}^6S\right) \rightarrow {}^4T_1\left({}^4P\right) = 18B + 7C \tag{3}$$

$$^6A_1\left({}^6S\right) \rightarrow {}^4T_1\left({}^4G\right) = -10Dq + 10B + 6C - \left(26B^2/10Dq\right) \tag{4}$$

$$^6A_1\left({}^6S\right) \rightarrow {}^4T_2\left({}^4G\right) = -10Dq + 18B + 6C - \left(26B^2/10Dq\right) \tag{5}$$

We have initially adjusted the transitions positions and, with the help of a computational program, extracted the energy parameters. The crystal field *Dq* parameter indicates the symmetry of impurity ion sites and the Racah parameters are related to orbital admixture of Fe^{3+} and ligand anions O^{-2}, that breaks selections rules and turns electronic transitions allowed [24, 25].

Results and discussion

We have identified three phases in the X-ray diffraction pattern (Fig. 1) of the sample: α-$LiGaSiO_4$, $LiGa_5O_8$ and δ-$Li_5GaSi_2O_8$ [27–29]. The most intense observed line corresponds to the maximum diffraction of $LiGa_5O_8$ [27]. The strongest α-$LiGaSiO_4$ line [28, 29] was observed with intensity of 13% and the most intense line of δ-$Li_5GaSi_2O_8$ with intensity 24% (both of them relative to the intensity of the $LiGa_5O_8$ line). The lithium gallium silicate α-$LiGaSiO_4$ [28, 29] has an ordered crystalline structure belonging to a space group with tetragonal symmetry and unit cell parameters $a=b=5.196$ Å and $c=6.186$ Å, isostructural to γ-$LiAlO_2$. All cations are tetrahedrally coordinated [28, 29]. The lithium gallium oxide $LiGa_5O_8$ [27] is a spinel, with two cation positions, one of them tetrahedral and the other octahedral. The unit cell belongs to the $O_h^7(Fd3m)$ group with cell parameter $a=8.221$ Å. The structure of the δ-$Li_5GaSi_2O_8$ compound is not fully determinate. The current literature contains information just on its diffraction data [28, 29].

In Fig. 2 we observe the photoacoustic average spectrum of the sample obtained with a frequency of 20 Hz after 20 scans at room temperature. The spectrum shows bands located in the visible region, between 350 nm and 700 nm. The $LiGa_5O_8$–$LiGaSiO_4$–$Li_5GaSi_2O_8$ system presents several

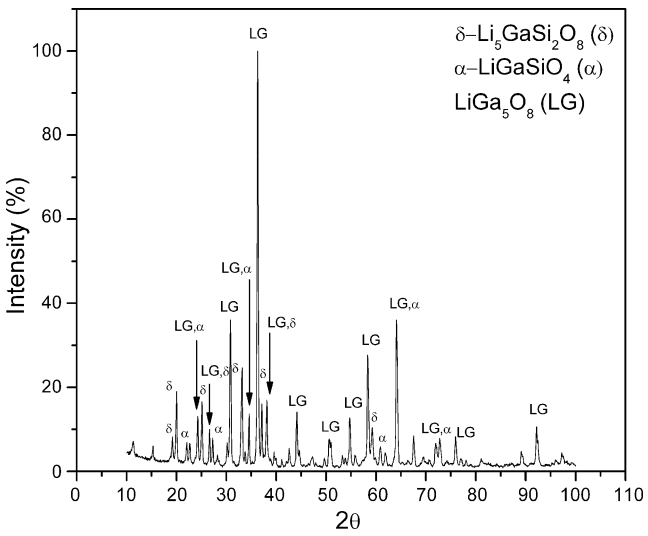

Fig. 1 XRD data of the prepared sample

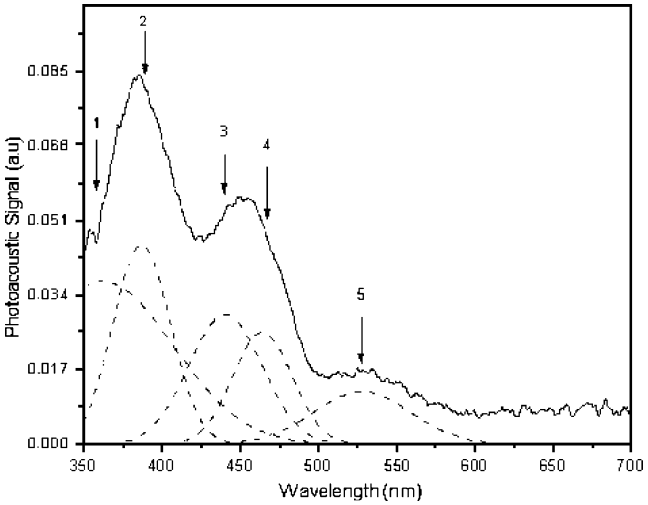

Fig. 2 Photoacoustic room temperature spectrum of Fe^{3+} in the $LiGa_5O_8$–$LiGaSiO_4$–$Li_5GaSi_2O_8$ system, at 20 Hz. *Numbers* indicate the transitions wavelength positions listed in Table 1 and the *dotted curves* are deconvoluted Gaussians

convenient Ga^{3+} ion sites for Fe^{3+} ion substitutional occupation. The photoacoustic spectrum shape is clear evidence that only Fe^{3+} was incorporated as impurity in the host system [30–33]. This technique, however, has not been enough to separate the optical centers. In spite of this, it allows us to know about the excited levels of the system. The assignments of energy levels are listed in Table 1. Initially, we used a computer program to adjust five Gaussians to the photoacoustic spectrum. The barycenters for these curves were assumed as "observed values" in Table 1. Taking the observed values as starting point, we have used a computational routine to solve the TS Eqs. (1) to (5) with simultaneous extraction of crystal field *Dq* and Racah *B* and *C* energy parameters. The "adjusted values" in Table 1 were values next to Gaussians barycenters from which we obtain the same values for energy parameters *Dq*, *B* and *C* in all five TS equations. The shift between the observed and adjusted values in Table 1 is explained by broadening and overlapping of absorptions bands. These characteristics turn very difficulty the correct determination of the energy transition positions in the spectrum. An important point of energy parameters is that they are averages values, however they can indicate the symmetry of the most common site in the studied system. The limited apparatus spectral response has prevented the observation of the band attributed to the ${}^6A_1({}^6S)\rightarrow{}^4T_1({}^4G)$ transition.

The energy TS diagrams [24, 25] are such that d^n (tetrahedral)$=d^{N-n}$ (octahedral), where N is the maximum number of electrons in the shell ($N=10$) and n is the number of electrons in the incomplete shell [24, 25]. Thus, the Fe^{3+} transitions are common to both octahedral and tetrahedral symmetries. The Fe^{3+} ions (d^5 electronic configuration) in sites with tetrahedral coordination present,

Table 1 Transitions and energy parameters of Fe^{3+} in the $LiGa_5O_8$–$LiGaSiO_4$–$Li_5GaSi_2O_8$ system

Band	Transition	λ (nm)		Energy (cm^{-1})		Energy parameters (cm^{-1})
		Observed values	Adjusted values	Observed values	Adjusted values	
1	$^6A_1(^6S)\rightarrow{}^4T_1(^4P)$	362	344	27,624	29,069	
2	$^6A_1(^6S)\rightarrow{}^4E(^4D)$	387	396	25,839	25,252	
3	$^6A_1(^6S)\rightarrow{}^4T_2(^4D)$	440	426	22,727	23,474	Dq=805
4	$^6A_1(^6S)\rightarrow{}^4E+{}^4A_1(^4G)$	464	484	21,551	20,661	B=656
5	$^6A_1(^6S)\rightarrow{}^4T_2(^4G)$	527	552	18,975	18,115	C=2,820
6	$^6A_1(^6S)\rightarrow{}^4T_1(^4G)$		686		14,577	

therefore, an energy level distribution similar to octahedral ones. However, the expected value for the crystal field parameter Dq for tetrahedral Fe^{3+} ions are around or below 800 cm^{-1} while for octahedral Fe^{3+} is higher than 1,000 cm^{-1} [34].

The obtained Dq value equals 805 cm^{-1}, allowing us to attribute the Fe^{3+} ion to tetrahedral sites. The obtained Racah parameter value, B=656 cm^{-1}, is lower than the 1,300 cm^{-1} free-ion B parameter, showing the principal covalent character of the Fe^{3+}-O^{-2} bond. The ratio C/B obtained from our experimental data is 4.3, very close to the value of 4.0 related in the literature [30–34].

Now we compare the ratios between energies at TS diagrams [24, 25] with the values obtained in this work. In TS d^5 electronic configuration diagram at Dq/B=1.23 it is expected that energy ratios follow: $^4T_1(^4P)/^4E(^4D)$=1.17; $^4E(^4D)/^4T_2(^4D)$=1.09; $^4T_2(^4D)/^4E+{}^4A_1(^4G)$=1.14; $^4E+{}^4A_1(^4G)/^4T_2(^4G)$=1.19 and $^4T_2(^4G)/^4T_1(^4G)$=1.24. Through the calculations performed with the energy values positions adjusted in this work we reach, following the same order as above: 1.15; 1.08; 1.14; 1.14 and 1.24. The results are consistent, and show that the energy attributions are correct. In fact, as broad bands barycenters are roughly estimated and the maximum associated difference between values was 4.2%, we can estimate that the precision in measurements was about 5%. Then the associated errors are acceptable.

In Fig. 3 we show the frequency dependence of the photoacoustic signal. We have used it to identify the dominant process in signal generation. Data correspond to the average of 20 frequency scans. The experimental procedure was to select the 393 nm wavelength for sample excitation and to vary the modulation frequency. The measurements were performed with 2 Hz intervals between 10 and 90 Hz. The signal exhibits a $f^{-0.94}$ dependence. Values close to $f^{-1.00}$ indicate that the photoacoustic spectra are generated mainly by thermal expansion effects on which the signal amplitude is proportional to the average temperature of the sample [32, 33, 35].

In Fig. 4 we see the phase signal dependence on the modulation frequency, that we have used to obtain the non-radiative lifetime τ=2.9 ms and the thermal diffusion time, τ_β=3.9 μs. The squares represent the average values of 20 measurements for each frequency. The continuous line is the theoretical fit using an equation presented elsewhere [30]. The procedure was, with the excitation radiation fixed in wavelength 393 nm, to change the modulation frequency with steps of 2 Hz and measure the phase that maximizes the signal, between 10 and 90 Hz.

The photoluminescence spectra at room temperature (RT—dotted line) and 4 K (full line), both of them obtained with excitation of 350 nm and with signal phase maximized to emission at 520 nm, are shown in Fig. 5. Often the Fe^{3+} luminescence bands in the red region of the visible spectrum are associated with an energy transition for the tetrahedral impurity ion while luminescence in the infrared region is associated with the octahedral ion [19]. The Fe^{3+} emissions from higher excited states (in blue-green region) are seldom, but were observed recently for both, tetrahedral and octahedral coordination [15, 36]. Then, the observed spectra were associated with spin-forbidden transitions of Fe^{3+} tetrahedrally coordinated by O^{-2} ligand anions in the

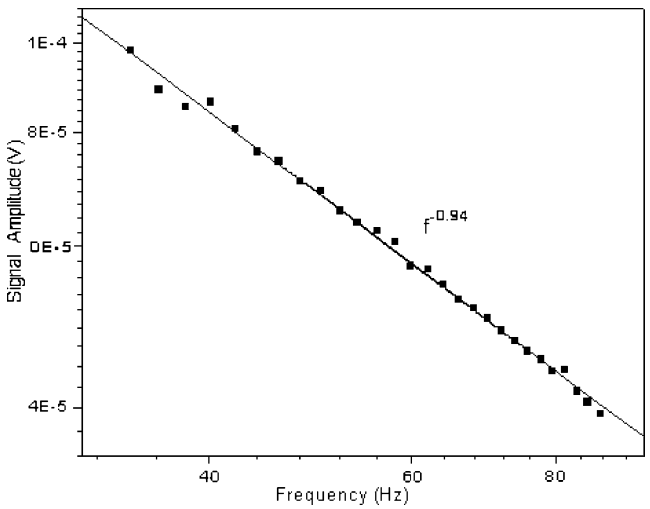

Fig. 3 Signal amplitude dependence on the modulation frequency of Fe^{3+} in the $LiGa_5O_8$–$LiGaSiO_4$–$Li_5GaSi_2O_8$ system, at room temperature and excitation wavelength of 393 nm

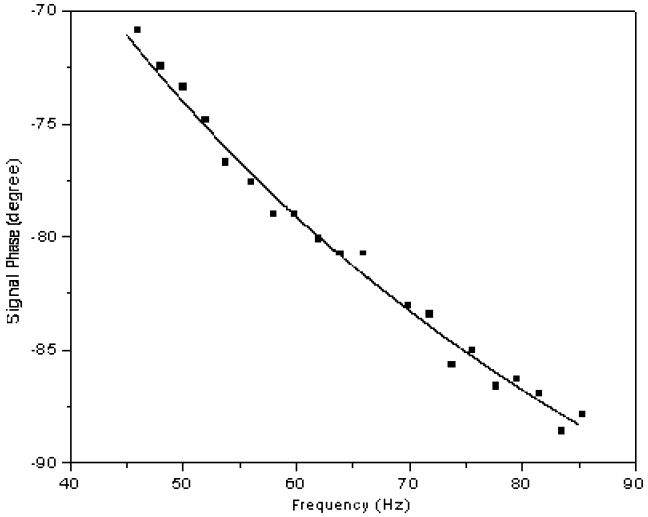

Fig. 4 Signal phase dependence with modulation frequency of Fe^{3+} in the $LiGaSiO_4$–$LiGa_5O_8$–$Li_5GaSi_2O_8$ system, at room temperature and excitation wavelength of 393 nm

$LiGa_5O_8$–$LiGaSiO_4$–$Li_5GaSi_2O_8$ system, or lithium gallium oxide–lithium gallium silicate system.

The room temperature (RT) lower energy band with barycenter at 725 nm, in Fig. 5, was associated with the $^4T_1(^4G)\rightarrow{}^6A_1(^6S)$ transition. The intermediate band located at 588 nm and the higher energy band located at 516 nm were associated with $^4T_2(^4G)\rightarrow{}^6A_1(^6S)$ and $^4E+{}^4A_1(^4G)\rightarrow{}^6A_1(^6S)$ transitions, respectively. In the 4 K spectrum (Fig. 5, solid line) the $^4T_1(^4G)\rightarrow{}^6A_1(^6S)$ and $^4T_2(^4G)\rightarrow{}^6A_1(^6S)$ transitions were slightly shifted to lower energies, by temperature action. In wavelength, to 737 nm and 630 nm, respectively.

The temperature lowering diminishes the impurity-ligand distance R while the crystal field parameter Dq depends [24, 25] upon R^{-5}. Thus, the Dq crystal field parameter increases when the sample temperature decreases.

As the energies of the $^4T_1(^4G)$ and $^4T_2(^4G)$ levels diminish while the Dq parameter increases, it should be expected that, at 4 K temperature, the energy transitions shift to lower energies, as observed. On the other hand, the $^4E+{}^4A_1(^4G)\rightarrow{}^6A_1(^6S)$ energy level value is independent of the Dq value. This is consistent with results observed in the spectra shown in Fig. 5. The barycenter position of the band in high energy regions is not changed with a temperature lowering, then this band in both (room and low temperatures) spectra was associated to the $^4E+{}^4A_1(^4G)\rightarrow{}^6A_1(^6S)$ transition.

The energy gaps between the excited states observed in this work were close to those observed by Z. Wen-Chen and collaborators [34]. In addition, the energy differences between electronic origins and absorption or luminescence maxima should be of comparable magnitude. The luminescence attributed to the $^4E+{}^4A_1(^4G)\rightarrow{}^6A_1(^6S)$ transition has its maximum at 516 nm (~19,380 cm^{-1}). The estimated electronic origin for $^6A_1(^6S)\rightarrow{}^4E+{}^4A_1(^4G)$ absorption from the peak fits in Fig. 2 is at 500 nm (20,000 cm^{-1}) with maximum intensity at 464 nm or 21,551 cm^{-1} (Table 1). The luminescent level, $^4E+{}^4A_1(^4G)$ is populated by absorption from the fundamental level $^6A_1(^6S)$ and by decay from the excited levels $^4T_1(^4P)$, $^4E(^4D)$ and $^4T_2(^4D)$. Therefore the luminescence from the $^4E+{}^4A_1(^4G)$ can be intense, in spite of the weaker absorption of this level.

All transitions occur between the fundamental state $^6A_1(^6S)$, with electronic configuration $t_2^3e^2$, and excited levels with t_2^4e electronic configuration, generating broad bands in the optical spectra. It is worth to mention that each band presents a non-homogeneous broadening which indicates the overlapping between two or more transitions. The radiative decay time (τ_R) was measured using the phase-shift method [37], which presents experimental errors of the order of 10%. Decay times of the $^4T_1(^4G)\rightarrow{}^6A_1(^6S)$ transition measured at RT and 4 K are about 2.0 ms. These decay times are average values, because it was not possible to verify the existence of two or more different occupation sites for Fe^{3+} ions. However, this value is similar for other tetrahedrally Fe^{3+}-doped systems [30, 31] and indicates that both infrared bands can be associated to the same $^4T_1(^4G)\rightarrow{}^6A_1(^6S)$ transition. Assuming that the luminescence temperature quenching is only due to non-radiative decays, the transition room temperature quantum efficiency (ϕ) can be estimated from the ratio $\phi=\tau_{RT}/\tau_{4K}$ [38, 39]. For room temperature, this calculation brings a Fe^{3+} emission quantum efficiency around 0.8, considering the experimental error. It can be seen from Fig. 5 that around 40% of the 4 K-emission integrated intensity remains at room temperature. This result shows that non-radiative decays processes are not strong enough to quench the luminescence at RT. This is an interesting result because our objective is the development of a broadband lumines-

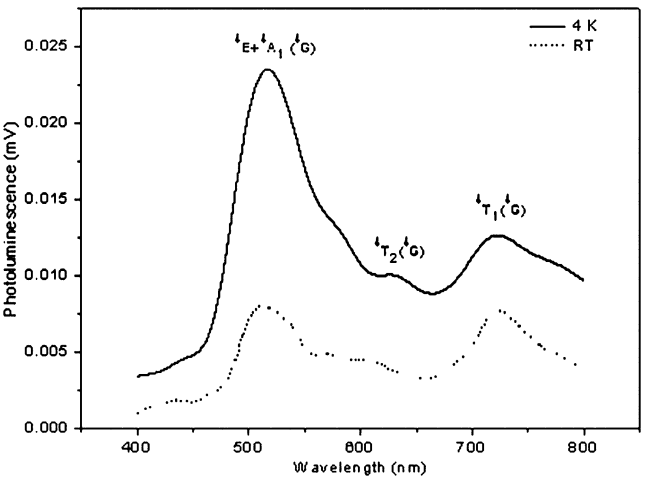

Fig. 5 Photoluminescence spectra excited with a wavelength of 350 nm for Fe^{3+} in the $LiGa_5O_8$–$LiGaSiO_4$–$Li_5GaSi_2O_8$ system, at RT (*dotted line*) and 4 K (*solid line*), with experimental apparatus prepared to intensify the blue-green signal

cent system with good optical quality and high quantum efficiency at room temperature.

The presence of Fe^{3+} in two or more site types in the $LiGa_5O_8$–$LiGaSiO_4$–$Li_5GaSi_2O_8$ system turns very difficult the correct interpretation of spectra. In order to explain the photoluminescence data, we have measured the low energy region separately and the results can be seen in Fig. 6. The spectrum, maximized at 725 nm, was obtained with the 488 nm excitation wavelength of an Ar^+ laser.

The non-homogeneous broadening could indicate the overlapping between two (or more) transitions, each of them associated with a different occupation site. This is expected because ions decay from energy levels associated with different sites, as in the $LiGa_5O_8$–$LiGaSiO_4$–$Li_5GaSi_2O_8$ system. To resolve the broad band, we use the phase that minimizes the emission at 725 nm. This result is presented in Fig. 7. Actually, the band at higher energies (a) was not completely erased, indicating again that bands are strongly overlapped. The remained band (b) was multiplied by 10 in order to compare with the others. The spectrum shows a broad band with barycenter at 820 nm, probably generated by the overlapping of two or more bands. Several tentative were performed to separate the emissions, but all of them failed. We attributed this fact to close radiative decay times for all the emissions, beyond our experimental capabilities.

Based upon X-ray results that indicate three compounds in the sample, we tried to adjust the photoluminescence spectrum (Fig. 6) through three curves associated with transitions from three different Fe^{3+} sites. The result is exhibited in Fig. 8, where we observe curves centered at 715 nm, 750 nm and 816 nm, with the convoluted curve exactly on the experimental data.

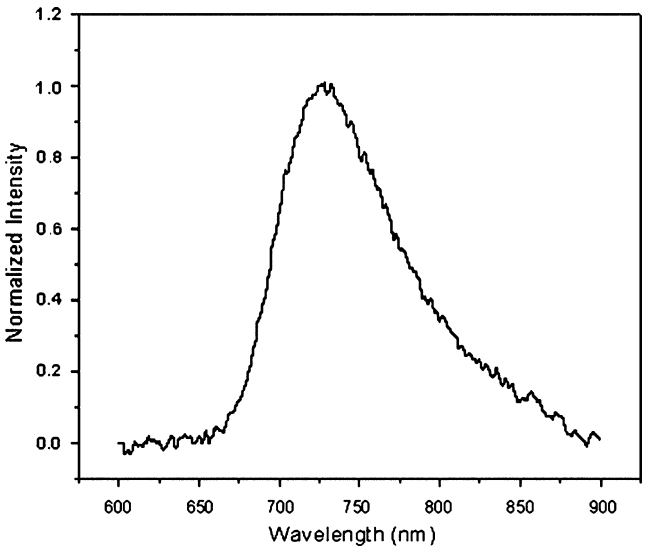

Fig. 6 Photoluminescence at room temperature of Fe^{3+} in the $LiGa_5O_8$–$LiGaSiO_4$–$Li_5GaSi_2O_8$ system, excited with the 488 nm line of an Ar^+ laser. The non-homogeneous broadening could indicate the overlapping of two (or more) transitions

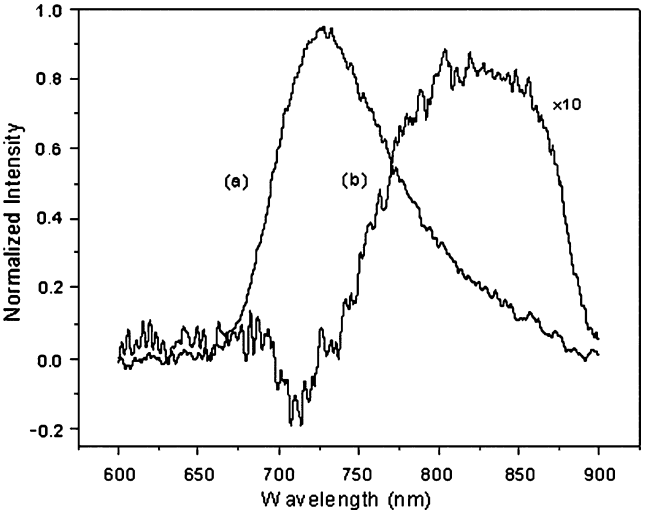

Fig. 7 Photoluminescence at room temperature of Fe^{3+} in the $LiGa_5O_8$–$LiGaSiO_4$–$Li_5GaSi_2O_8$ system, excited with the 488 nm line of an Ar^+ laser. **a** The spectrum shown in Fig. 5; **b** spectrum obtained with a line at 725 nm quenched by an appropriated signal phase choice. The cut-off at 870 nm is due to the photomultiplier spectral detection limits

By comparison with the results presented in a previous work [31], the band at 715 nm was attributed to the $LiGa_5O_8$:Fe^{3+} compound. The problem that remains is to identify the broad band at 816 nm. Actually, it is not possible to resolve completely this band because the related optical transitions are strongly overlapped.

The excitation spectra of the $^4T_1(^4G)$ energy level at RT and (dotted line) 4 K (full line) are shown in Fig. 9. The observed transitions were assigned (see Table 2) and the energy parameters calculated with the procedure used to analyze photoacoustic data.

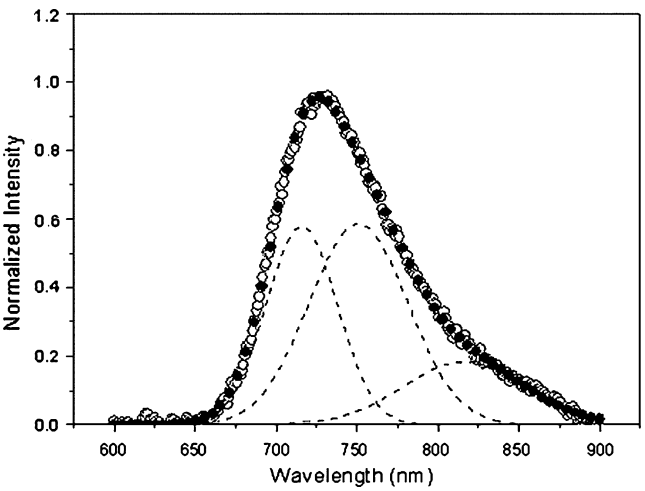

Fig. 8 Photoluminescence room temperature spectrum of Fe^{3+} in the $LiGa_5O_8$–$LiGaSiO_4$–$Li_5GaSi_2O_8$ system, showing experimental luminescence data (*white circles*), convoluted Gaussian (*black circles*) and adjusted Gaussians (*dotted lines*)

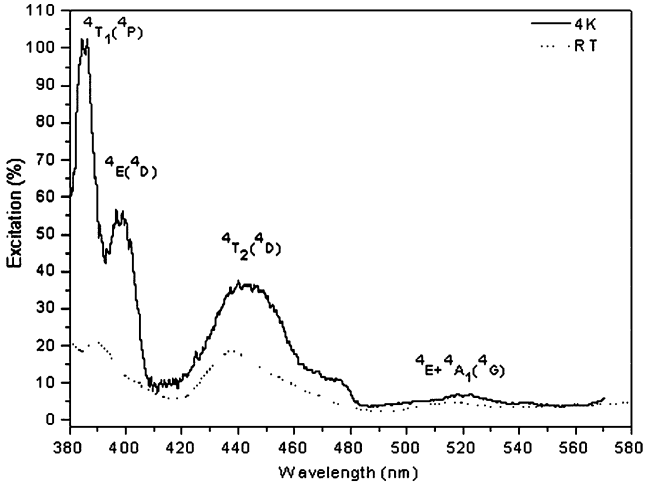

Fig. 9 Excitation at RT (*dotted line*) and 4 K (*full line*) of Fe^{3+} in the $LiGa_5O_8$–$LiGaSiO_4$–$Li_5GaSi_2O_8$ system

The transitions from $^6A_1(^6S)$ to $^4T_2(^4G)$ and $^4T_1(^4G)$ energy levels are not observed due to instrumental limitations, but their positions were predicted from TS matrices [24, 25]. The small structure at 475 nm was attributed to transitions overlapping from different sites in the sample. We have not found evidences indicating that this structure could be associated with undesirable impurities as Cr^{3+}, or valences, as Fe^{2+}. The $^6A_1(^6S)\rightarrow{}^4E+^4A_1(^4G)$ transition is observed at 516 nm and at 518 nm, in RT and 4 K excitation spectra, respectively, while the emission $^4E+^4A_1(^4G)\rightarrow{}^6A_1(^6S)$ occurs at 516 nm. As can be seen in TS energy diagrams for d^5 electronic configuration [24, 25], the $^4E+^4A_1(^4G)$ energy level is not dependent on the crystal field parameter Dq value. Then, it is expected the $^6A_1(^6S)\leftrightarrow{}^4E+^4A_1(^4G)$ emission or absorption (excitation) to occur always at the same wavelength position in spectra. This fact is confirmed by our experimental results and assignments.

Finally, we now compare the ratio between energies at TS diagrams and between the values obtained from excitation measurements. In TS diagram for d^5 electronic configuration [24, 25] at $Dq/B\sim1.00$ the ratios between energy levels are: $^4T_1(^4P)/^4E(^4D)=1.16$; $^4E(^4D)/^4T_2(^4D)=1.06$; $^4T_2(^4D)/^4E+^4A_1(^4G)=1.14$; $^4E+^4A_1(^4G)/^4T_2(^4G)=1.11$ and $^4T_2(^4G)/^4T_1(^4G)=1.18$. The ratios calculated with our adjusted values to the RT spectrum were, respectively: 1.11; 1.07; 1.16; 1.11 and 1.23. For low temperature data we obtain 1.11; 1.07; 1.16; 1.11; 1.24, in the same order. The results here are also consistent, and show once more that the energy attributions are correct.

Conclusions

The photoluminescence, excitation and photoacoustic absorption of the $LiGa_5O_8$–$LiGaSiO_4$–$Li_5GaSi_2O_8$ system were investigated. The photoacoustic and excitation spectra shapes are characteristic of Fe^{3+} transitions. Non-homogeneous band broadenings indicate that a strong transition overlapping occurs. From the theoretical adjust of photoacoustic data we extracted the crystal field Dq=805 cm^{-1} and B=656 cm^{-1} and C=2,820 cm^{-1} Racah parameters. From the B value lower than the free ion value (1,300 cm^{-1}) we deduce that the Fe^{3+}-O^{-2} bond presents a character more covalent than ionic. This fact leads to a mixture between Fe^{3+} and O^{-2} energy levels, breaking the spin multiplicity selection rule and generating the observed spectra. The dependence of the photoacoustic signal on the modulation frequency is $f^{-0.94}$, which indicates that thermal expansion is the dominant effect in the photoacoustic signal generation and that the signal amplitude is proportional to the average sample temperature. From the excitation data the obtained crystal field Dq and Racah parameters B and C at room temperature and 4 K were (in cm^{-1}) 705, 678, 2,596 and 713, 689 and 2,558,

Table 2 Excitation data of Fe^{3+} in the $LiGa_5O_8$–$LiGaSiO_4$–$Li_5GaSi_2O_8$ system for the $^4T_1(^4G)\rightarrow{}^6A_1(^6S)$ emission at room temperature (RT) and 4 K, located at 720 nm

	Transition	$^4T_1(^4P)$	$^4E(^4D)$	$^4T_2(^4D)$	$^4E+^4A_1(^4G)$	$^4T_2(^4G)$	$^4T_1(^4G)$	Energy parameters (cm^{-1})
Excitation RT	λ observed (nm)		390	437	516	559		Dq=705 B=678 C=2,596
	λ adjusted value (nm)	367	408	438	506	561	692	
	Energy observed (cm^{-1})		25,641	22,883	19,380	17,889		
	Energy adjusted (cm^{-1})	27,248	24,510	22,831	19,763	17,825	14,450	
Excitation 4 K	λ observed (nm)	386	398	443	518			Dq=713 B=689 C=2,558
	λ adjusted value (nm)	368	408	438	508	564	702	
	Energy observed (cm^{-1})	25,908	25,125	22,573	19,305			
	Energy adjusted (cm^{-1})	27,174	24,510	22,831	19,685	17,730	14,245	

respectively. We can observe the photoluminescence spectra at RT and 4 K spread from 400 nm to 800 nm. We have identified three non-homogeneous broad bands at both RT and 4 K temperature spectra. The bands at lower energies were associated with the $^4T_1(^4G) \rightarrow {}^6A_1(^6S)$ transition, the intermediate band was attributed to $^4T_2(^4G) \rightarrow {}^6A_1(^6S)$ and the higher energy band was related to $^4E + {}^4A_1(^4G) \rightarrow {}^6A_1(^6S)$ transitions. These bands are related with the overlap of Fe^{3+} transitions because it is expected that impurity ions occupy different sites in the sample. From the integrated intensity of RT and 4 K spectra we calculated that 40% of the 4 K-emission integrated intensity remained at room temperature. No result was found in optical spectra related with other impurity further than Fe^{3+}. The results indicate that this system is a promising media for applications as broad band luminescent sources.

Acknowledgements The authors thank FAPERJ, CAPES, CNPq and FINEP by partial financial support and CBPF, by the X-ray measurements.

References

1. Zhou S, Feng G, Wu B et al (2007) Intense infrared luminescence in transparent glass-ceramics containing β-Ga_2O_3:Ni^{2+} nanocrystals. J Phys Chem C 111(20):7335–7338 doi:10.1021/jp068370i
2. Zhao X, Wang X, Chen B et al (2007) Novel Eu^{3+}-doped red-emitting phosphor $Gd_2Mo_3O_9$ for white-light-emitting-diodes (WLEDs) application. J Alloy Comp 433(1–2):352–355 doi:10.1016/j.jallcom.2006.06.096
3. Han T, Jaque F (2007) Optical stability of the Cr^{3+} centers in co-doped stoichiometric and congruent $LiNbO_3$:Cr:Mg. Opt Mater 29 (8):1041–1043 doi:10.1016/j.optmat.2006.04.002
4. Grinberg M, Suchochi A (2007) Pressure-induced changes in the energetic structure of the $3d^3$ ions in solid matrices. J Lumin 125 (1–2):97–103 doi:10.1016/j.jlumin.2006.08.018
5. Santana GC, de Mello ACS, Valério MEG et al (2007) Scintillating properties of pure and doped BGO ceramics. J Mater Sci 42(7):2231–2235 doi:10.1007/s10853-006-1319-6
6. Clarke DR, Tolpygo VK, Gentleman M (2004) Luminescence-based characterization of protective oxides: from failure mechanisms to non-destructive evaluation. Mater Sci Forum 461–464: 621–630
7. Chan TS, Liu RS, Baginsky I (2008) Synthesis, crystal structure, and luminescence properties of a novel green-yellow emitting phosphor $LiZn_{1-x}PO_4$:Mn_x for light emitting diodes. Chem Mater 20(4):1215–1217 doi:10.1021/cm7028867
8. Yang WJ, Luo L, Chem TM et al (2005) Luminescence and energy transfer of Eu- and Mn-coactivated $CaAl_2Si_2O_8$ as a potential phosphor for white-light UVLED. Chem Mater 17 (15):3883–3888 doi:10.1021/cm050638f
9. Pires AM, Davolos MR (2001) Luminescence of europium (III) and manganese(II) in barium and zinc orthosilicate. Chem Mater 13(1):21–27 doi:10.1021/cm000063g
10. Bordallo HN, Wang X, Hanif KM et al (2002) Structure determination and a vibrational study for the hexagonal elpasolite Cs_2NaGaF_6:Cr^{3+}. J Phys Condens Matter 14(47):12383–12390 doi:10.1088/0953-8984/14/47/312
11. Sosman LP, Abritta T, Pereira AC et al (1994) Photoacoustic spectroscopy of Co^{2+} in $ZnGa_2O_4$ and $MgGa_2O_4$. Chem Phys Lett 227(4–5):485–489 doi:10.1016/0009-2614(94)00856-6
12. Su FN, Deng Z (2006) Influence of chemical environment on the optical properties in transition metal ions doped materials. J Fluoresc 16(1):43–46 doi:10.1007/s10895-005-0031-2
13. Sosman LP, da Fonseca RJM, Dias Tavares Jr A et al (2006) Photoluminescence and optical absorption of Cs_2NaScF_6:Cr^{3+}. J Fluorescence 16(3):317–323 doi:10.1007/s10895-005-0045-9
14. Short MA (2005) Polarization effects in the excitation and emission of Fe^{3+} in orthoclase and their relevance to the determination of lattice sites of unknown defects. J Phys Condens Matter 17(1):205–220 doi:10.1088/0953-8984/17/1/019
15. Kornylo A, Jankowska-Frydel A, Kuklinsky B et al (2004) Spectroscopic properties of $ZnWO_4$ single crystal doped with Fe and Li impurities. Radiat Meas 38(4–6):707–710 doi:10.1016/j.radmeas.2004.03.003
16. Monteiro T, Boemare V, Soares V et al (2003) Photoluminescence and damage recovery studies in Fe-implanted ZnO single crystals. J Appl Phys 93(11):8995–9000 doi:10.1063/1.1573341
17. Abritta T, Barros FS (1988) Luminescence and photoacoustic measurements of $LiAl_5O_8$:Fe^{3+}. J Lumin 40–41:187–188 doi:10.1016/0022-2313(88)90150-0
18. Abritta T, Barros FS (1985) Luminescence of Fe^{3+} in single crystals of $LiAl_5O_8$. J Lumin 33(2):141–146 doi:10.1016/0022-2313(85)90012-2
19. Bingham PA, Parker JM, Searle TM et al (2007) Local structure and medium range ordering of tetrahedrally coordinated Fe^{3+} ions in alkali–alkaline earth–silica glasses. J Non-Cryst Solids 353(24–25):2479–2494 doi:10.1016/j.jnoncrysol.2007.03.017
20. O'Connor G, McDonagh C, Glynn TJ (1991) Luminescence from Fe^{3+} ions in octahedral sites in $LiGa_5O_8$. J Lumin 48–49:545–548 doi:10.1016/0022-2313(91)90189-3
21. Kutty TRN, Nayak M (1999) Cation coordination and Fe^{3+} luminescence in $LiAlO_2$ polymorphs prepared by a hydrothermal method. Mater Res Bull 34(2):249–262 doi:10.1016/S0025-5408(99)00014-8
22. Melamed NT, Maria Neto J, Abritta T et al (1981) A comparison of the luminescence of $LiAl_5O_8$:Fe and $LiGa_5O_8$:Fe-II. Fe^{3+} in octahedral sites. J Lumin 24–25:249–252 doi:10.1016/0022-2313(81)90264-7
23. Pott GT, McNicol BD (1973) The luminescence of Fe^{3+} and Cr^{3+} in α-gallia. J Lumin 6(3):225–228 doi:10.1016/0022-2313(73)90122-1
24. Tanabe Y, Sugano S (1954a) On the absorption spectra of complex ions I. J Phys Soc Jpn 9(5):753–766 doi:10.1143/JPSJ.9.753
25. Tanabe Y, Sugano S (1954b) On the absorption spectra of complex ions II. J Phys Soc Jpn 9(5):766–779 doi:10.1143/JPSJ.9.766
26. Bush TS, Catlow CRA, Chadwick AV et al (1992) Studies of cation dopant sites in metal oxides by EXAFS and computer-simulation techniques. J Math Chem 2(3):309–316 doi:10.1039/jm9920200309
27. JCPDS-ICDD, card 38-1371.
28. Quintana P, West AR (1989) Compound formation and phase equilibria in the system Li_4SiO_4–$LiGaSiO_4$. J Solid State Chem 81 (2):257–270 doi:10.1016/0022-4596(89)90013-3
29. Chavira E, Quintana P, West AR (1987) Phase-equilibria and compound formation in the system $LiGaSiO_4$–SiO_2. Br Ceram Trans J 86(5):161–165
30. Sosman LP, Abritta T, Amaral MR et al (1998) Optical properties of $LiGaTiO_4$:Fe^{3+}. Solid State Commun 105(2):135–138 doi:10.1016/S0038-1098(97)00329-3
31. McShera C, Colleran PJ, Glynn TJ et al (1983) Luminescence study of $LiGa_{5-x}Fe_xO_8$. J Lumin 28(1):41–52 doi:10.1016/0022-2313(83)90024-8

32. dos Santos DR, Toledo R, Massunaga MSO et al (2003) Photoacoustic spectroscopy applied to the study of clay soils. Rev Sci Instrum 74:355–357 doi:10.1063/1.1518553
33. da Silva MAFM, Pedro SS, Sosman LP (2008) Fe^{3+} concentration dependence of photoacoustic absorption spectroscopy on $ZnGa_2O_4$ ceramic powders. Spectrochim Acta Part A Mol Biomol Spectrosc 69:338–342 doi:10.1016/j.saa.2007.04.003
34. Wen-Chen Z, Xiao-Xuan W, Lv H et al (2007) An alternative interpretation of the optical spectra for Fe^{3+}-doped $KTaO_3$ crystals. J Lumin 126(1):91–93 doi:10.1016/j.jlumin.2006.05.012
35. Hill RJ, Craig JR, Gibbs GV (1979) Systematics of the spinel structure type. Phys Chem Miner 4(4):317–339 doi:10.1007/BF00307535
36. Zotov N, Yanev Y, Piriou B (2002) Time-resolved luminescence of Fe^{3+} and Mn^{2+} ions in hydrous volcanic glasses. Phys Chem Miner 29(4):291–299 doi:10.1007/s00269-001-0233-3
37. Martin JE, Shea-Rohwer LE (2006) Lifetime determination of materials that exhibit a stretched exponential luminescent decay. J Lumin 121(2):573–587 doi:10.1016/j.jlumin.2005.12.043
38. Kück S (2001) Laser-related spectroscopy of ion-doped crystals for tunable solid-state lasers. Appl Phys B 72(5):515–562
39. Wenger OS, Güdel HU (2001) Optical spectroscopy of $CrCl_6^{3-}$ doped $Cs_2NaScCl_6$: broadband near-infrared luminescence and Jahn–Teller effect. J Chem Phys 114(13):5832–5841 doi:10.1063/1.1352730